Distributed Multipole Models for Design and Control of PM Actuators and Sensors

Hungsun Son, *Student Member, IEEE*, and Kok-Meng Lee, *Fellow, IEEE*

***Abstract*—Design and control of multi-degree-of-freedom (DOF) electromagnetic actuators require a good understanding of the magnetic fields, and involve real-time calculation of magnetic forces. This paper presents a method to derive distributed multipole (DMP) models for characterizing the magnetic field and torque of permanent magnet (PM) based devices. The DMP method, which offers magnetic-field solutions in closed form, inherits many advantages of the dipole model originally conceptualized in the context of physics, but provides an effective means to account for the shape and magnetization of the physical magnet. Three practical applications are given to demonstrate the DMP models for design of PM-based actuators and sensing systems. The magnetic fields and forces calculated using DMP models have been validated by comparing against numerical and experimental results which show excellent agreement.**

***Index Terms*—Actuator, magnetic field, permanent magnet, sensor, spherical motor, torque model.**

I. Introduction

MANY automated processing equipment, machine tools, mobile vehicles (such as car wheels [1], [2], propellers for boats, helicopter, or underwater vehicle), and gyroscopes require orientation control of a rotating shaft. Growing interest in fuel-cell technology and low-cost electric vehicles has motivated a number of researchers to develop application-oriented in-wheel or multi-degree-of-freedom (DOF) spherical motors. Design optimization and real-time control of these motors require the formulation of its forward and inverse torque models.

Existing techniques for analyzing electromagnetic fields, and for design and control of a multi-DOF PM-based actuator rely primarily on three approaches; namely, analytic solutions to Laplace equation, numerical methods, and lumped-parameter analyses with some form of magnetic equivalent circuits [3]. The possibility of obtaining an analytic solution is often remote for devices with complex geometry. Perturbation theory and linear superposition can, sometimes, render a difficult problem solvable. However, even if an analytic solution is achievable, it often results in a series of space harmonics of nonelementary functions [4], [5], which must be computed if a numeric solution to the problem is desired. Motivated by the ability of using digital computers to make repetitious computation, Harrington [6] proposed the concept of matrix methods (also known as the method of moments) as a numerical approach to solve for the magnetic field. Commonly used in antenna design and magnetic wave propagation analysis (see for examples, [7] and [8]), the method of moments (MM) assumes the dipole moments inside a magnet cancelling each other, thereby reducing the governing equation to an integral equation of surface charges. The resulting boundary value problem can then be solved with surface (volume) discretization using the MM, which provides a compact matrix formulation. However, computation time tends to grow due to the need of fully populated matrix inversion and fine discretization for numerical accuracy and stability. During the last four decades, several other computational methods for solving magnetic field problems including finite element (FE), boundary element, finite difference, and mesh-free methods have been very well developed. Numerical methods (such as the FE method) offer a good field prediction for accurate computation of the magnetic torque [9], [10]. However, demanding computation limits these numerical methods to offline calculation. In order to obtain closed-form solutions for design optimization and motion control of electromagnetic actuators, real-time computations have largely relied on lumped parameter approaches that generally yield only first-order accuracy. These approaches have difficulties in achieving both accuracy and low computation time simultaneously.

An alternative method is based on the concept of a magnetic dipole (originally suggested by Fitz Gerlad in 1883) as a tool to characterize the magnetic potential fields. Two models, 1) a single dipole or doublet at the origin and 2) two individual poles with one at each end, have been widely used to analyze the magnetic field at a sufficiently large distance for applications [11]–[13] such as electromagnetic wave propagation (antenna dynamics) and geomagnetism (earth polarization). However, both models generally give a poor approximation when the length scale of the field is very small because the source and sink are essentially singular (infinite field density); the errors increase as air gaps become smaller. For reasons including compact formulation and solutions that depict intuitive magnetic fields, many researchers (e.g., [14] and [15]) continue to develop dipole models to analyze actuator designs involving permanent magnets. Nedelcu *et al*. [14] used a magnetic dipole to describe the field of a PM-based device, where each PM is modeled as a doublet. While the model in [14] provides concise formulae for calculating the field and energy flow, it has difficulties to obtain an accurate solution. Visschere [15] later pointed out a number of mistakes by comparing the dipole approximation in [14] against an analytical 2-D magnetic field solution of a PM. The existing single dipole model (or the mathematical theory of a

Manuscript received May 10, 2007; revised September 27, 2007. Recommended by Technical Editor M. E. Benbouzid. This work was supported in part by the Georgia Agricultural Technology Research Program (ATRP) and in part by the U.S. Poultry and Eggs Association.

The authors are with Woodruff School of Mechanical Engineering, Georgia Institute of Technology, Atlanta, GA 30332 USA (e-mail: kokmeng.lee@me.gatech.edu).

Color version of one or more of the figures in this paper are available online at http://ieeexplore.ieee.org.

Digital Object Identifier 10.1109/TMECH.2008.918544

doublet) is often studied in the context of physics and is valid only for needle-like magnets; thus, it has very limited applications in modern actuator design. This has led us to develop a new method to derive closed-form solutions for efficient design and robust control of modern actuators.

The remainder of this paper offers the following:

1) We present the DMP method. Unlike the MM that offers a numerical procedure, the DMP method provides precise calculation of magnetic fields in closed form. The simplicity of this method offers an advantage for real-time applications.
2) We illustrate the procedure of developing a DMP model for characterizing the magnetic field, and validate it by comparing the calculated magnetic fields and forces against known solutions whenever possible, and/or published numerical simulations and experimental results.
3) Three practical applications of the DMP method are given. The 1st example demonstrates the design of PM-based repulsion actuators for noncontact rotation of moving devices at high speed. The 2nd example simulates the transient response of a spherical motor. The 3rd example illustrates the DMP method for real-time orientation sensing applications.

II. DMP Field Models in Closed-Form

For electromechanical actuators involving both permanent magnets (PMs) and electromagnets (EMs), the Lorenz force equation is commonly used to calculate the magnetic force exerted on current-carrying conductors

$$\mathbf{F} = -\oint \mathbf{B} \times I d\ell \ \text{ where } \ I = -\iint \mathbf{J} \cdot d\mathbf{S} \qquad (1a)$$

where ℓ is the normalized current direction vector. In (1a), the current density vector $\mathbf{J}$ is directly used in the calculation, and thus, it is not necessary to compute the magnetic flux generated by the current loop. Thus, the Lorenz force calculation involves only modeling the $\mathbf{B}$ fields of the permanent magnets.

Alternatively, magnetic forces can be calculated using the Maxwell stress tensor

$$\mathbf{F} = \oint_{\Omega} \boldsymbol{\Gamma} d\Omega \text{ where } \boldsymbol{\Gamma} = \frac{1}{\mu_0}\left(\mathbf{B}(\mathbf{B}\cdot\mathbf{n}) - \frac{1}{2}B^2\mathbf{n}\right) \qquad (1b)$$

where Ω is an arbitrary boundary enclosing the body of interest; $\mathbf{n}$ is the normal vector at the material interface. In computing the force using the surface integration (1b), $\mathbf{B}$ is the total field (of all the PMs and EMs). As will be shown in an illustrative example, (1b) can be used only when PMs are used for actuation.

The solution to the force equation (1a) or (1b) requires solving the magnetic field. The method presented here derives closed-form magnetic-field solutions for design of PM-based applications that satisfy the following assumptions: the field is continuous and irrotational; and the medium is homogeneous and linear without saturation. Historically, ferromagnetic cores were commonly used in electromagnetic actuators. The widely available high-coercive rare-earth PMs at low cost have begun to change that usage, and air-cored electromagnets are now commonly seen in ironless motors. For this reason, we focus on examples without any magnetic conducting boundary.

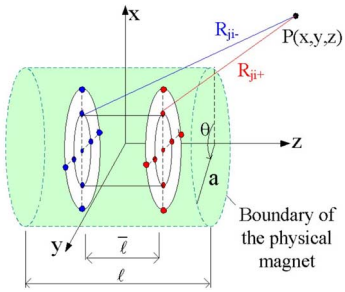

Fig. 1. DMP model of a cylindrical magnet.

However, the DMP method can be extended to account for the effects of magnetic conducting boundary by incorporating the image method [16]. The irrotational field $\nabla \times \mathbf{B} = 0$ enables us to define a scalar magnetic potential Φ such that the magnetic field intensity $\mathbf{H}$ is given by

$$\mathbf{H} = -\nabla\Phi \text{ and } \mathbf{B} = \mu_0\mathbf{H} \qquad (2a,b)$$

where μ_0 is free space permeability. Since the field is continuous $\nabla \cdot \mathbf{B} = 0$, $\nabla^2\Phi = 0$, the solution to Laplace's equation satisfying the field for a pole [17] is given by

$$\Phi = \frac{(-1)^j}{4\pi R} m \qquad (3)$$

where m is the strength of the pole; j takes the value 0 or 1 designating that the pole is a source or a sink, respectively; and R is the distance from the pole to the field point.

Since a single pole does not physically exist alone in a magnet field, we define a *dipole* as a pair of source and sink separated by a distance $\bar{\ell}$. An effective method to approximate flux paths of a PM is to use multiple dipoles to account for the shape of the physical magnet. For design and control of PM-based devices, we seek the field solution outside the physical region of the magnet, particularly near its boundary.

Cylindrical PMs and EMs are commonly used. Some analytical and experimental results are also available for model validation. They are used here for clarity to illustrate the DMP modeling procedure. However, the method can be readily extended to PMs of customized shape. Fig. 1 shows the DMP model of a cylindrical PM (radius a, length ℓ, and magnetization $\mathbf{M} = M_o\mathbf{e}_z$), where k circular loops (each with radius $\bar{a}_j$) of n dipoles are parallel to $\mathbf{M}$. The k loops are uniformly spaced

$$\bar{a}_j = aj/(k+1) \quad \text{at} \quad z = \pm\bar{\ell}/2$$
$$\text{where} \quad j = 0, 1, \ldots, k \qquad (4)$$
$$0 < \bar{\ell} < \ell. \qquad (5)$$

In Fig. 1, R_{ji+} and R_{ji-} are the distances from the ith source and sink in the jth loop to any point $P(x, y, z)$, respectively

$$R_{ji\pm}^2 = (x - \bar{a}_j\cos i\theta)^2 + (y - \bar{a}_j \sin i\theta)^2 + (z \mp \bar{\ell}/2)^2. \qquad (6)$$

For a cylindrical PM, the field is uniform circumferentially, and thus, $m_{ji} = m_j$. In addition, the following constraint is imposed on n to minimize the field variation in the θ direction:

$$\left.\frac{\text{Max}\left[\Phi(\theta)\right] - \text{Mean}\left[\Phi(\theta)\right]}{\text{Mean}\left[\Phi(\theta)\right]}\right|_{r=a,z=\ell/2} \times 100\% \le \varepsilon_\theta \qquad (7)$$

where ε_θ is a specified (positive) error bound.

Since Laplace's equation is linear, the potential $\Phi(x, y, z)$ can be obtained by summing the individual contributions

$$\Phi = \frac{1}{4\pi}\sum_{j=0}^{k} m_j \sum_{i=1}^{n_k}\left(\frac{1}{R_{ji+}} - \frac{1}{R_{ji-}}\right)$$

where

$$n_k = \begin{cases} 1 & \text{if } j = 0 \\ n & \text{if } j \neq 0 \end{cases}. \tag{8}$$

Similarly, the magnetic flux density at P can be found from (2)

$$\mathbf{B} = \frac{\mu_o}{4\pi}\sum_{j=0}^{k} m_j \sum_{i=1}^{n_k}\left(\frac{\mathbf{a}_{Rji+}}{R_{ji+}^2} - \frac{\mathbf{a}_{Rji-}}{R_{ji-}^2}\right). \tag{9}$$

Since $\nabla(1/R) = -\mathbf{a}_R(1/R^2)$ where $\mathbf{a}_R\ (= \mathbf{R}/R)$

$$\frac{\mathbf{a}_{Rji\pm}}{R_{ji\pm}^2} = -\frac{(x - \bar{a}_j\cos i\theta)\,\mathbf{a}_x + (y - \bar{a}_j \sin i\theta)\,\mathbf{a}_y + \left(z \pm \bar{\ell}/2\right)\mathbf{a}_z}{[(x - \bar{a}_j\cos i\theta)^2 + (y - \bar{a}_j \sin i\theta)^2 + \left(z \pm \bar{\ell}/2\right)^2]^{3/2}}.$$

The unknowns (k, n, $\bar{\ell}$, and m_j where $j = 0, \ldots, k$) in the DMP model are solved by minimizing the error function (10a) subject to constraints imposed by the magnet geometry and a limited set of known field solutions (as fitting points):

$$E = \int_z \left[\Phi(z) - \Phi_A(z)\right]^2\, dz \tag{10a}$$

where $\Phi_A(z)$ is the analytical solution along $\mathbf{M}$ (or the z-axis). The general expression of Φ_A in 3-D space from a magnetic pole at $\mathbf{R}'$ (x', y', z') to a field point $\mathbf{R}(x, y, z)$ is given in [17]

$$\Phi_A = \frac{1}{4\pi}\int_V \frac{-\nabla\cdot\mathbf{M}}{|\mathbf{R} - \mathbf{R}'|}dV + \frac{1}{4\pi}\int_S \frac{\mathbf{M}\cdot\mathbf{n}}{|\mathbf{R} - \mathbf{R}'|}dS \tag{10b}$$

where $\mathbf{n}$ is the unit surface normal. The 1st integral in (10b) is a volume integral over the body volume V, while the 2nd is a surface integral over the body boundary surface S. The corresponding magnetic flux density can be found using (2). For the uniformly magnetized PM shown in Fig. 1, the 1st term in (10b) is zero and the potential and flux density along the z-axis can be solved analytically in closed form

$$\frac{\Phi_A(Z)}{M_o\ell} = \frac{1}{4}[(A_- - |B_-|) - (A_+ - |B_+|)] \tag{11}$$

$$\frac{B_A(Z)}{\mu_o M_o} = \frac{1}{2}\left[\frac{|B_+|}{A_+} - \frac{|B_-|}{A_-} + c\right],$$

where

$$c = \begin{cases} 0 & \text{if } |Z| \geq 1 \\ 2 & \text{if } |Z| < 1 \end{cases} \tag{12}$$

$$Z = \frac{z}{\ell/2}, \gamma = \frac{a}{\ell/2}, A_\pm = \sqrt{\gamma^2 + B_\pm^2}, \text{ and } |B_\pm| = |Z \pm 1|.$$

For a given specified residual magnetic flux density, we have

$$\mathbf{B}(z = \ell/2) = \mathbf{B}_A(z = \ell/2) = -\mu_o\ \nabla\Phi_A|_{z=\ell/2} \tag{13}$$

TABLE I
VALUES OF THE PARAMETERS ($k = 1, n = 6$)

	OD= ℓ mm	$\mu_o M_o$ Tesla	$\delta = \bar{\ell}/\ell$	M $(T/m^2)\times 1.0e\text{-}4$	Error %
A	**19.05**	1.12	0.5141	m_o=-0.424; m_{1i}=1.151	0.998
B	**12.7**	1.35	0.5136	m_o=-0.229; m_{1i}=0.618	1.00

where $\mathbf{B}$ is given in (9). Since (10a) accounts for the potential field along the magnetization axis, the remaining $(k \times n + 1)$ constraints are constructed from (8) and (9) along two other orthogonal directions. For PM-based actuator applications, the specified Φ values are evaluated over an appropriate magnet surface. To avoid the singularity at $\mathbf{R} = \mathbf{R}'$, we choose

$$|R| = \lim_{\varepsilon\to 0}\left(|R'||_{\substack{\text{point}\\ \text{at surface}}} + \varepsilon_R\right)$$

where ε_R is a small positive number. The procedure for modeling a PM is summarized as follows:

Step 1) Compute Φ_A and $\mathbf{B}_A$ analytically along the magnetization vector from (11) and (12), respectively.

Step 2) Generate an initial set of spatial grid points (k, n).

Step 3) Formulate (8) and (9) in terms of the unknowns, $\bar{\ell}$ and m_{ji}.

Step 4) Find $\bar{\ell}$ and m_{ji} by minimizing (10a) subject to (13) and constraints from other known field points with the aid of (8) or (9). Error computed by (10a) is saved.

Step 5) Check if the condition (7) is met. If no, increase k or n, and repeat from *Step 3*. If yes, the optimal parameters (k, n, $\bar{\ell}$, and m_{ji}) can be obtained by minimizing (10a) using *Step 4*.

III. VALIDATION OF DMP MODELS

To illustrate and validate the DMP model for magnetic force computation, we model two PMs and denote here as DMP (A) and DMP (B); both have a unity aspect ratio (or $\gamma = 2a/\ell = 1$) but different sizes and magnetization.

A. DMP Model of a Permanent Magnet

Using the MATLAB optimization toolbox, the parameters, k, n, δ, m_j, and m_o were solved for $\gamma = 1$ by minimizing (10a) subject to constraints (7) where $\varepsilon_\theta = 0.05\%$, (8), and (13). For a PM with constant $\mathbf{M}_o$, the known field points, $\Phi = \Phi_A\,(0, y, \ell/2)$ in (8), can be numerically integrated from (10b). Mathematically, the field is singular at the surface, the Φ_A values for (10b) and (11) are solved numerically with $|\mathbf{R}'| + 10^{-6}$; no significant difference in results was found when $\varepsilon_R \leq 10^{-3}$. The DMP model for the PM with unity aspect ratio is summarized in Table I, where the error is defined as

$$\%\text{Error} = 100 \times \frac{\int_{\ell/2+10^{-6}}^{\infty} |\Phi(z) - \Phi_A(z)|\ dz}{\int_{\ell/2+10^{-6}}^{\infty} |\Phi_A(z)|}\, dz.$$

The simulated fields using DMP models are compared with exact solutions in Fig. 2. The effects of k (number of loops) and n (number of dipoles per loop) are simulated in Fig. 3. Some observations are summarized as follows:

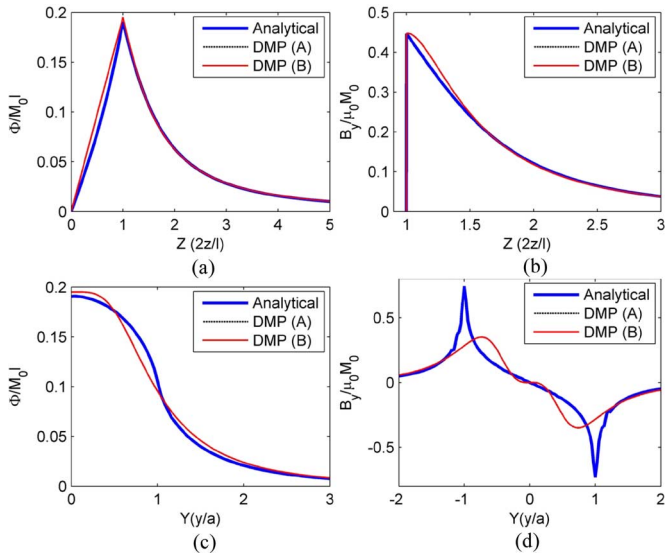

Fig. 2. Potential and flux density along Y- and Z-axes ($n = 6$ and $k = 1$). (a) $\Phi(Z)$. (b) $B(Z)$. (c) $\Phi(Y)$. (d) $B(Y)$.

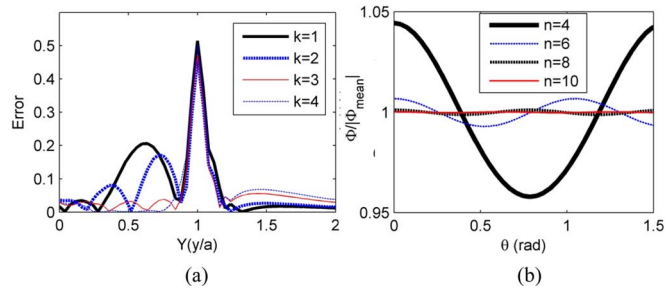

Fig. 3. Effect of n and k on modeling errors of PM with $\gamma(2a/\ell) = 1$. (a) Effect of k on corner error ($n = 6$). (b) Effect of n on variation in $\theta(k = 1)$.

1) The normalized potential and density fields, $\Phi_A(Z)/(M_o\ell)$ and $B_A(Z)/(\mu_o M_o)$, depend on the aspect ratio γ only. This is consistent with (11) and (12), respectively.
2) Fig. 2 shows that the exact solutions agree well with the field solutions modeled using only seven dipoles ($n = 6$ and $k = 1$).
3) The discrepancy in Fig. 2(d) primarily occurs around the corner of the PM; it can be reduced by using more loops, as shown in Fig. 3. Similarly, the variations in θ can be reduced by increasing the number of dipoles in each of the loops.

It is worth noting that the DMP method provides the field solutions in closed form, and does not require mesh generation, pre-, and postprocessing generally needed in the FE method.

B. Force Computation With DMP Models

We examine the effect of DMP models on the magnetic force by computing the repulsive force between two identical magnets (modeled using multiple dipoles) using Maxwell stress tensor (1b). The computed forces are compared in Fig. 4 against analytical solutions and published experimental and numerical data

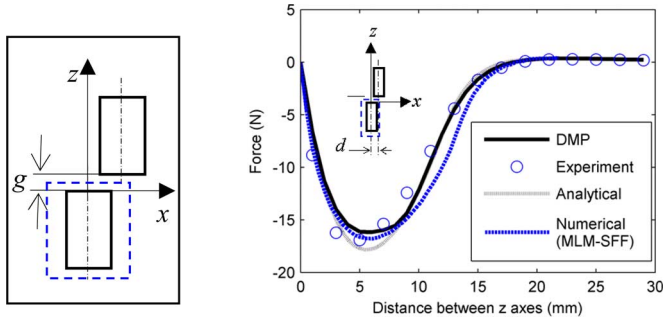

Fig. 4. Repulsion between two PMs as a function of displacement d [19] ($R = L = 6.35$ mm, air gap $= 0.5$ mm, and $\mu_0 M_0 = 1.35$ T).

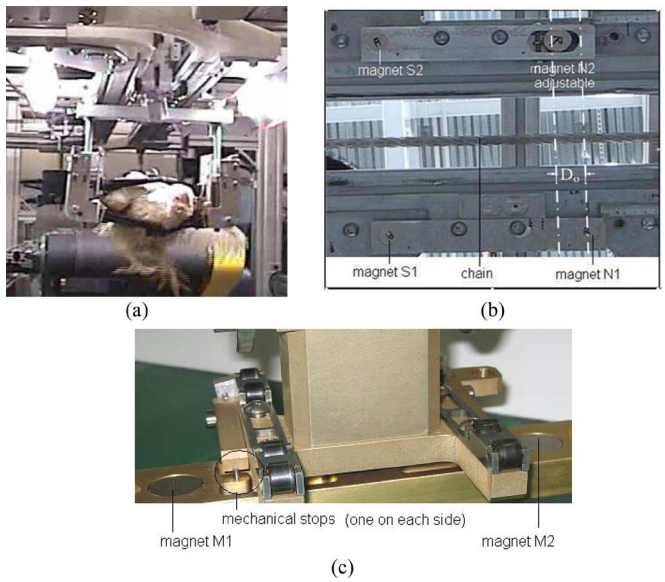

Fig. 5. Reorientation and alignment in live-bird transfer system. (a) Setup. (b) PM fixed on underside of the track. (c) PM on grasper.

in [19]. The comparisons are remarkably close, validating the DMP model as well as demonstrating the effectiveness of its closed-form field solution.

IV. Example 1: (Repulsion Actuators)

In transferring live products for meat processing, repetitive reorientation and alignment are often required so that the grasped products face a unique direction for subsequent handling. Fig. 5(a) shows a PM-based mechanism, which uses high coercive PM as energy-efficient contact-free actuators for product orientation. This example applies DMP models to predict the magnetic fields and forces involved in the orientation control, which must be achieved smoothly without compromising the production line speed. The parameters used in this simulation are based on the live-bird transfer system shown in Fig. 5(a) [20] so that computed results can be validated experimentally. The reorientation/alignment mechanism (which cradles a live product with a grasper) travels along a high-speed production line. The actuating system consists of six identical PMs. Four of these ($N1/N2$ with an offset D_o, and $S1/S2$) are fixed on the underside of the track, and the other two ($M1/M2$) are

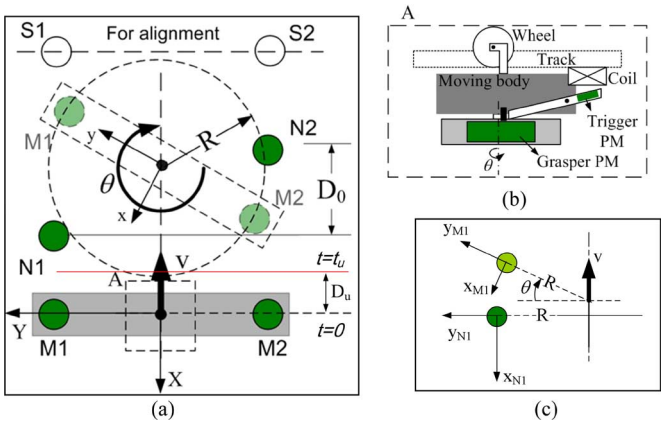

Fig. 6. Schematics illustrating the reorientation/alignment mechanism. (a) Layout of permanent magnets. (b) Side view of A in Fig. 5(d). (c) Coordinate systems.

embedded in the moving grasper, as shown in Fig. 5(b) and (c), respectively.

The operational principle of the magnetic actuating system is illustrated in Fig. 6(a), where the shading of the magnets indicates their polarities; $S1/S2$ has opposite polarity of $N1/N2$ and $M1/M2$. The PM-trigger on the grasper (moving at a constant speed v along a motorized chain) is initially locked mechanically to prevent it from any rotation, as illustrated in Figs. 5(c) and 6(b). Upon receiving a command from a vision system [20] to make an orientation correction, the coil activation unlocks the PM-trigger allowing the device to rotate the grasper (in θ direction) by the repulsive force (of two PM of like-polarities) to a specified orientation (defined by the pair of alignment PM of opposite polarities) within an often very short cycle time while the grasper moves continuously. The only energy input required in this PM-based device is a finite pulse of energy to unlock the trigger, which relocks by gravity.

In order to predict and verify the computed trajectory of the grasper using DMP models, we compute the net repulsive torques and simulate the motion of the rotating magnet M_1. The coordinate of M_1 is given by

$$\mathbf{x}_{\mathrm{M1}} = \begin{pmatrix} \cos\theta & \sin\theta & 0 \\ -\sin\theta & \cos\theta & 0 \\ 0 & 0 & 1 \end{pmatrix} \left(\mathbf{x}_{N1} + \begin{bmatrix} vt - D_u \\ R \\ 0 \end{bmatrix} \right) - \begin{pmatrix} 0 \\ R \\ 0 \end{pmatrix} \tag{14}$$

where $\mathbf{x}_{N1}$ and $\mathbf{x}_{M1}$ are the position vectors of the fixed magnet $N1$ and the moving magnet $M1$, as defined in Fig. 6(c); and D_u is the location at which the trigger is unlocked. The dynamics of the grasper motion $\theta(t)$ is given by

$$I\ddot{\theta} + c\dot{\theta} = T_z \tag{15}$$

where I is the grasper inertia about the rotational axis; c is the friction coefficient determined experimentally; and T_z is the net torque acting on the rotating grasper by the permanent magnets.

The DMP parameters (derived using the method given in Section II) for the PM are summarized in Table II. With the

TABLE II
PARAMETERS OF THE PM-BASED ORIENTATION CORRECTION MECHANISM

Grasper	I=0.0316kg-m^2; c= 0.01N-s/m; v=0.45m/s
Actuator configuration	D_o=25mm; $2R$=175mm
(X, Y) cord. of N1, N2, S1, S2	(−0.035m, R), (−0.06m, −R), (−0.235m, ±R)
Vert. gap between M_i and N_i	g=6.25mm
Neodymium PM (grade N38)	B_r=1.24Tesla; $2a$=25mm; ℓ =12.5mm

DMP model of the magnet:

$\gamma = 2a/\ell$	n	k	$\delta = \overline{\ell}/\ell$	$m_i(T/m^2)\times 1.0e\text{-}3$, $i=0,1,2$	%Error
0.25	6	1	0.9445	0.0091, 0.9097	4.66
		2	0.3105	0.1291, 0.0087, 0.3277	2.47

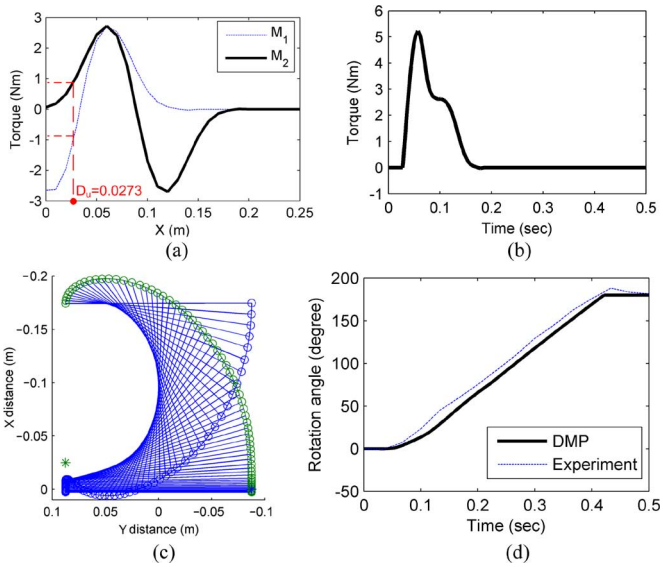

Fig. 7. Experimental setup and simulated trajectories $\theta(t)$. (a) Torque on the locked grasper. (b) Net torque on the rotating grasper. (c) Trajectory of the moving PM. (d) Comparison between simulated and video-recorded data.

magnetic flux density $\mathbf{B}$ calculated from the DMP models, the torque can be computed using the Maxwell stress tensor (1b).

The computed torque and simulated trajectory of the moving magnets are shown in Fig. 7. Fig. 7(a) shows the torques acting on a locked grasper (due to the forces between $N1$ and $M1$ and between $N2$ and $M2$). Initially, a large negative torque acts on the grasper as M_1 approaches N_1; unlocking at this moment would require overcoming a significantly large static friction. However, as M_2 moves into the range of N_2, the net torque (algebraic sum of the two individual torques) acting on the grasper gradually reduces, passes through zero, and becomes very positive. The optimal instant to unlock for a clockwise rotation is when the net torque is zero, and thus, the static friction is a minimum. From Fig. 7(a), this location corresponds to $t = t_u$ or $D_u = 27.3$ mm. Fig. 7(b) and (c) shows the net driving torque and trajectory of the moving grasper (which is unlocked at D_u during the travel). In Fig. 7(c), the two moving magnets M_1 and M_2 are marked as *circles*, which move with respect to the fixed magnet N_1 marked as *asterisk*. As compared to Fig. 7(d), the simulated trajectory θ (t) agrees well with experimental data obtained using a 3-charge-coupled device CCD digital camera.

The offset D_o used in the aforementioned simulation has been based on an existing system that aims at completing a 180°

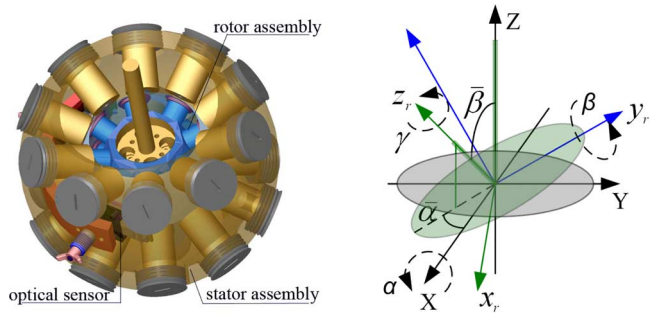

(a) (b)

Fig. 8. Spherical motor. (a) CAD Model (SWM [18]). (b) Rotor inclination in the XYZ frame.

rotation within a specified distance and time. With the DMP-modeled field and torque, the offset D_o can be optimized by maximizing the mechanical power $T_z\dot{\theta}$ subject to constraints (14) and (15). Using the Matlab optimization toolbox, the optimal D_o can be found to be 19.9 mm.

V. Example 2: (Spherical Motor Control)

DMP models can be used to derive the forward and inverse torque models for motion control of a spherical motor. The forward model computes the torque, and along with the rotor dynamics given in Appendix A, simulates the rotor motion. The inverse model that computes an optimized set of currents to provide the torque for tracking the desired trajectory, however, must be controlled in real time. As will be shown, the DMP models provide a means to derive a closed-form version of the inverse model for real-time current optimization while retaining the full-torque model to predict the motion of the spherical motor.

Fig. 8 shows a computer-aided design (CAD) model of a spherical wheel motor (SWM) [18], a modified design of variable-reluctance spherical motors (VRSM) [9]. Unlike a VRSM, where the rotor PMs and stator EMs are placed on locations following the vertices of a regular polygon, the PMs and EMs of an SWM are equally spaced on layers of circular planes such that their magnetization axes pass radially through the motor center. In addition, they are grouped in pairs; every two pole pairs form a plane providing symmetrical forces electromechanically.

A. Design Configuration of a Spherical Motor

In rotor coordinates (x, y, z), the magnetization axes of the m_r PM pole-pairs are given by (16)

$$\mathbf{r}_i = (-1)^{i-1}\left[\cos\phi_r\cos\theta_{ri} \quad \cos\phi_r\sin\theta_{ri} \quad \sin\phi_r\right]^T \tag{16}$$

where $i = 1, 2, \ldots, m_r$; and $\theta_{ri} = (i-1)\theta_r$. Similarly, the m_s EM pole pairs in the stator frame (XYZ) are given by (17). In (17), ϕ_r and ϕ_s are the inclination angles between the magnetization axes of the PM and EM pole-pairs and the XY plane, respectively,

$$\mathbf{s}_j = \left[\cos\phi_s\cos\theta_{sj} \quad \cos\phi_s\sin\theta_{sj} \quad \sin\phi_s\right]^{\mathrm{T}} \tag{17}$$

where $j = 1, 2, \ldots, m_s$; and $\theta_{si} = (i-1)\theta_s$. Unlike m_s which may be odd or even, m_r, is always an even number.

The inclination of a continuously spinning rotor is commonly described in terms of ZYZ Euler angles $(\bar{\alpha}, \bar{\beta}, \gamma)$ as it can be easily visualized; see Fig. 8(b). This representation, however, has singularities at $\alpha = 0, \pm\pi$ making it difficult to compute numerically. Thus, the XYZ Euler angles (α, β, γ) are used for numerical computation with the coordinate transformation

$$\alpha = -\sin^{-1}\left(\sin\bar{\alpha}\sin\bar{\beta}\right) \tag{18a}$$

and

$$\beta = \sin^{-1}\left(\sin\bar{\alpha}\cos\bar{\beta}/\cos\alpha\right). \tag{18b}$$

For a structure with linear magnetic properties, the magnetic field of the spherical motor is obtained by summing over the magnetic fields of the rotor PMs in stator frame (inertia frame) with the coordinate transformation (19).

$$\mathbf{x}_s = \mathbf{L}_{sr}\mathbf{L}_{ri}\mathbf{x}_{ri} \tag{19}$$

where $\mathbf{x}_{ri}$ represents the local coordinate frame of the ith PM defined in Fig. 8(b); $\mathbf{L}_{ri}$ describes the transformation from $\mathbf{x}_{ri}$ to $\mathbf{x}_r$

$$\mathbf{L}_{\mathbf{r}i} = \begin{pmatrix} \cos\phi_r & \sin\theta_{ri}\sin\phi_r & -\cos\theta_{ri}\sin\phi_r \\ -\sin\phi_r & \sin\theta_{ri}\cos\phi_r & -\cos\theta_{ri}\cos\phi_r \\ 0 & \cos\theta_{ri} & \sin\theta_{ri} \end{pmatrix}$$

and $\mathbf{L}_{sr}$ from $\mathbf{x}_r$ to $\mathbf{x}_s$, $\mathbf{L}_{sr}$, shown in the equation found at the bottom of the page.

Equation (19) facilitates the torque calculation in stator frame.

B. Torque Calculation

The resultant torque of the spherical motor has the form

$$\mathbf{T} = \left[T_X \quad T_Y \quad T_Z\right]^T = [\mathbf{K}]\,\mathbf{u} \tag{20}$$

where

$$\mathbf{K}\left(\in \mathbb{R}^{3\times m_s}\right) = \left[K_1 \quad \cdots \quad K_j \quad \cdots \quad K_{m_s}\right] \tag{20a}$$

and

$$\mathbf{u} = \left[J_1 \quad \cdots \quad J_j \quad \cdots \quad J_{m_s}\right]^T \tag{20b}$$

$$\mathbf{L}_{sr} = \begin{pmatrix} \cos\gamma\cos\beta & \cos\gamma\sin\alpha\sin\beta & -\cos\gamma\cos\alpha\sin\beta + \sin\gamma\sin\alpha \\ -\sin\gamma\cos\beta & \cos\bar{\alpha}\cos\phi - \sin\gamma\sin\alpha\sin\beta & \sin\gamma\cos\alpha\sin\beta + \cos\gamma\sin\alpha \\ \sin\beta & -\sin\alpha\cos\beta & \cos\alpha\cos\beta \end{pmatrix}$$

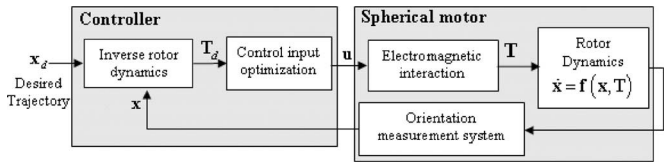

Fig. 9. Closed-loop control of the spherical motor.

In (20a), the vector K_j $\left(\in \mathbb{R}^{3\times 1}\right)$ characterizes the torque contribution of the jth EM. In terms of rotor orientation

$$K_j = \mathbf{L}_{sj}\left(\oint_{\mathrm{EM}} \mathbf{R}\times(\mathbf{J}_j/|\mathbf{J}_j|)\times\left[\sum_{i=1}^{2m_r}\mathbf{B}_i(\alpha,\beta,\gamma)\right] r\,dr\,d\theta\,d\ell\right) \tag{21}$$

where $\mathbf{B}_i \in \mathbb{R}^{3\times 1}$ is the magnetic flux density of the ith PM; $\mathbf{R}$ and r are the position vector and the radius of current conductor, respectively; and $\mathbf{L}_{sj}$ is the coordinate transformation from $\mathbf{x}_{sj}$ (the local coordinate frame of the jth EM) to $\mathbf{x}_s$, which has the same form as $\mathbf{L}_{\mathbf{r}i}$ but with the angles in (17).

C. Control System Analysis

As illustrated in Fig. 9, the forward model (20) simulates the rotor motion for a given set of current inputs. The inverse model computes an optimized set of currents providing the required torque $\mathbf{T}_d$ in order to track the desired trajectory $\mathbf{x}_d$ in real time.

1) Inverse Torque Model in Closed Form: The torque characteristic vector (20) is orientation dependent, and the volume integral (21) must be evaluated numerically in real time. In order to reduce (20) to a tractable form so that an optimized set of current inputs can be computed and implemented in real time, it is desired to express the inverse model in closed form. It has been shown in [9] that for a spherical motor with linear magnetic properties, the torque generated by the interaction of one stator EM pole pair with m_r rotor PM pole pairs can be calculated by summing up its individual interaction with m_r rotor pole pairs. Thus, the torque vector due to the interaction of one stator polepair and m_r rotor pole pairs can be evaluated as follows:

$$\hat{K}_j = \begin{cases} -\sum_{k=1}^{m_r}\left\{\hat{f}(\varphi)|_{\varphi=\varphi_{jk}}\dfrac{\mathbf{s}_j\times\mathbf{r}_k}{|\mathbf{s}_j\times\mathbf{r}_k|}\right\}, & \text{if } \mathbf{s}_j\times\mathbf{r}_k\neq 0 \\ 0, & \text{if } \mathbf{s}_j\times\mathbf{r}_k = 0 \end{cases} \tag{22}$$

where $\hat{f}(\varphi)$ is a curve-fit function derived from (23) as a separation angle φ between a PM pole-pair and an EM pole-pair, as shown in Fig. 8(a); and

$$\varphi_{jk} = \cos^{-1}\left(\mathbf{s}_j\cdot\mathbf{r}_k\right)/\left(|\mathbf{s}_j|\,|\mathbf{r}_k|\right). \tag{23}$$

The actual current input vector $\mathbf{u}$ is found by minimizing the control input energy consumption

$$J = \frac{1}{2}\mathbf{u}^T[\mathbf{W}]\mathbf{u} \tag{24}$$

subject to the desired torque constraint

$$\mathbf{T}_d = \begin{bmatrix}\hat{K}_1 & \cdots & \hat{K}_j & \cdots & \hat{K}_{m_s}\end{bmatrix}\mathbf{u}$$

TABLE III
ROTOR PARAMETERS

Parameters	Design A [9]	Design B [18]
Rotor		
Diameter mm(inch)	76.2 (3)	76.2 (3)
PM, number of	6 (1 layer)	16 (2 layers of 8)
Magnetization axis	$\gamma_r = 0^o$; $\delta_r = 60^o$	$\gamma_r = 20^o$; $\delta_r = 45^o$
$\mu_o M_o$ (Tesla)	1.12	1.35
OD= 2ℓ mm (inch)	19.05 (0.75)	12.7 (0.5)
Aspect ratio $\gamma(2a/\ell)$	1	1
Moment of inertia (kg-mm^2)	$I_a = 700$; $I_t = 35$	$I_a = 60.6$; $I_t = 38.6$
Offset of mass centre	$\bar{r} = 0$	$\bar{r} = 0$
Stator		
Air-gap, mm	0.762	
EM, number of	10 (2 layers of 5)	20 (2 layers of 10)
Magnetization axis	$\gamma_s = 26^o$; $\delta_s = 36^o$	
ID/OD/ 2ℓ mm	9.53/12.7/25.4	9.53/19.05/25.4
Number of coil turns	600	1050
29AWG wire resistance (Ω)	6.46	10.51

where $[\mathbf{W}] \in R^{m_s\times m_s}$ is a positive-definite weighting matrix. Provided that the control currents are kept within limits, the optimal $\mathbf{u}$ can be solved using Lagrange multipliers. The optimal solution, in closed form, can be written as

$$\mathbf{u} = [\mathbf{K}]^T\left([\mathbf{K}]\,[\mathbf{K}]^T\right)^{-1}\mathbf{T}_d. \tag{25}$$

In implementation, saturation limits are imposed on the controller to ensure the current inputs are within the amplifier limitations. The eventual stability of the system depends on whether the spherical motor can generate the desired torque.

2) PD Controller: For completeness, the rotor dynamics are given in Appendix A. Using the Lyapunov stability analysis, it can be shown that the desired torque for a PD controller can drive the spherical rotor from its initial state to a specified final state

$$\mathbf{T_d} = [\mathbf{K_p}]\tilde{\mathbf{x}}_1(\mathbf{t}) + [\mathbf{K_d}]\tilde{\mathbf{x}}_2(\mathbf{t}) \tag{26}$$

where $\tilde{\mathbf{x}}_1(\mathbf{t}) = \mathbf{q_d} - \mathbf{q}(\mathbf{t})$ and $\tilde{\mathbf{x}}_2(\mathbf{t}) = \dot{\mathbf{q}}_\mathbf{d} - \dot{\mathbf{q}}(\mathbf{t})$ define the tracking error and its derivative, respectively; and $\mathbf{q}=[\bar{\alpha}\quad\bar{\beta}\quad\gamma]^T$ is the orientation vector of Euler angles. In applications, the closed-form inverse model (25) is used in real-time control while the full torque model (20) is retained to faithfully predict the motion of the spherical motor.

D. Simulation Results

We compare the simulation results against published experimental data for two different designs; Design A (VRSM [9]) and Design B (SWM [18]) in Fig. 8. In both designs, the coils are air cored and other parameters used in the following simulations are given in Table III. To examine the effect of the DMP models on magnetic force prediction, we compute the torque exerted on the EM pole pairs under the influence of the magnetic field due to the rotor PMs using (20), where the magnetic flux density is given by (9) along with the DMP models in Table I.

To validate the force computation, we simulate the torque for Design A, since numerical solutions from ANSYS, a commercial FE package, are available for comparison [9]. Both the

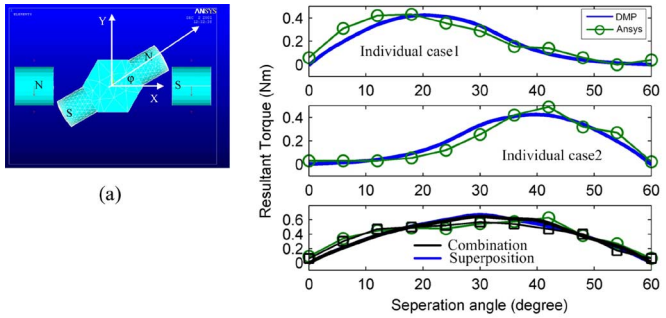

Fig. 10. Torque computation using the DMP model. (a) Torque computation between a PM- and an EM pole pairs. (b) Comparison of torque computation.

TABLE IV
COMPUTATIONAL TIME (SECONDS)

DMP		ANSYS	
Cases 1 and 2	Case 3	Cases 1 and 2	Case3
0.0128T(16.14)	0.0132T(16.9)	0.5484T(702.0)	T=1280.0

DMP-based and ANSYS models are simulated in 3-D space with the same modeling parameters.

Three cases were simulated. In Case 1, we compute the torque generated by the interaction between the EM pole-pair $\mathbf{s_1}$ and the PM pole-pair $\mathbf{r_1}$, as shown in Fig. 10(a), where the pole locations are defined in (16) and (17). Case 2 is identical to Case 1 except that the interaction is between $\mathbf{s_1}$ and $\mathbf{r_2}$. Case 3 was performed to determine whether the principle of superposition holds, which compares the superposition of the two individual cases against the torque calculated with $\mathbf{s_1}$ and the combined $\mathbf{r_1}$ and $\mathbf{r_2}$. In each of these cases, the stator coils are given a current of 4 A. As shown in Fig. 10(b), the torques computed using the DMP models as a function of rotor position agree well with the ANSYS results. ANSYS took about 12 min to compute Cases 1 and 2, and 20 min for Case 3 using a Windows-based PC (dual-core processor 2.21 GHz CPU and 1 GB memory), while the DMP-based models require less than 17 s to compute each of the cases, as compared in Table IV.

The time needed to calculate the magnetic torque can be further reduced by modeling the multilayer EM as an equivalent single-layer EM or PM [21], where the DMP method provides an essential basis. In the FE method, the free space must be bounded; particularly in 3-D, the computation cost increases drastically with the size of the free space. This, along the distortion of automatically generated FE meshes, contributes to some discrepancy (of less than 5% difference) between the two models. The mesh distortion could be the cause of the FE error (offset) when the separation angle is zero.

Once the magnetic field is characterized, the torque can be computed from (20). Fig. 11 compares the DMP-modeled results against those obtained using ANSYS for the torque between a PM pole pair and an EM pole pair of Design B shown in Fig. 8(a). In addition to the need for a relatively large free space to enclose the magnetic field, ANSYS depends significantly on the mesh resolution for its accuracy. Unlike ANSYS results, where few data are available, the DMP-based torque model is smooth and

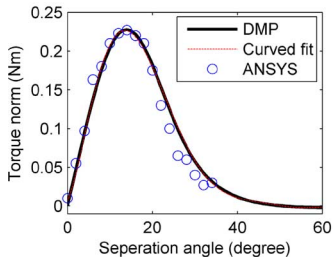

7^{th} order polynomial fit function:

$$\hat{f}(\varphi) = \sum_{k=0}^{7} c_k \varphi^k$$

where $c_0 = -53.18$; $c_1 = 232.51$; $c_2 = -402.68$; $c_3 = 343.74$; $c_4 = -142.27$; $c_5 = 20.61$; $c_6 = 1.25$; and $c_7 = 0.01$

Fig. 11. Torque between a PM- and an EM pole pair.

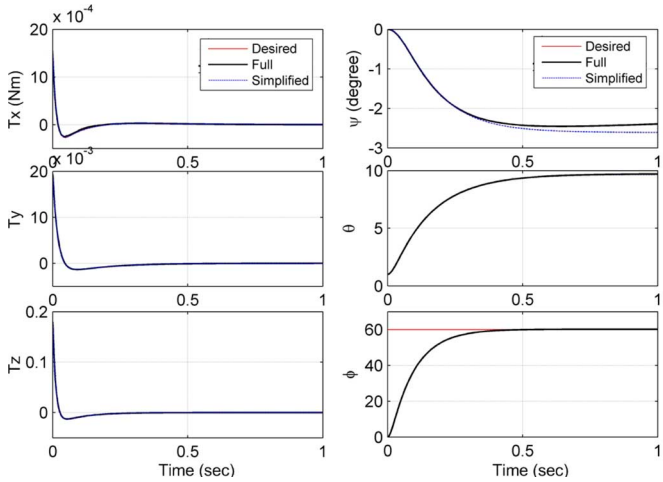

Fig. 12. Step response of spherical motor (Design B).

TABLE V
MAXIMUM PERCENTAGE ERROR

Torques (%)			Angles (%)		
Tx	*Ty*	*Tz*	ψ	θ	ϕ
9.52	3.94	4.76	8.9	1.6	2.3

can be easily curve-fitted. With 7th order polynomial curve fit, the average error is less than 0.02%.

We simulate, as an illustration, the closed-loop control system using the DMP-modeled torque. The measurement system is assumed to have no dynamics. For a specified $\mathbf{T}_d$, the optimized set of current inputs is given by (25), where $\hat{f}(\varphi)$ is given in Fig. 11. With the following PD gains

$$[\mathbf{K}_p] = \begin{bmatrix} 500 & 0 & 0 \\ 0 & 300 & 0 \\ 0 & 0 & 500 \end{bmatrix} \quad \text{and} \quad [\mathbf{K}_d] = 50\mathbf{I}$$

where $\mathbf{I}$ is 3×3 identity matrix, results for a step change in rotor orientation from its initial upright position ($\alpha = \beta = \gamma = 0°$) to a final state ($\alpha = 0°, \beta = 10°$ and $\gamma = 60°$) are given in Fig. 12. To examine the effect of the curve-fit function based on DMP models, we compare the full model (21) and the simplified closed-form solution (22) in modeling the forward torque. As shown in Fig. 12 and Table V, the comparisons show excellent agreement with less than 10% error in both the computed torque and the simulated motions.

We also investigate the effect of pole-pair configurations on the closed-loop control by comparing the current inputs, torques,

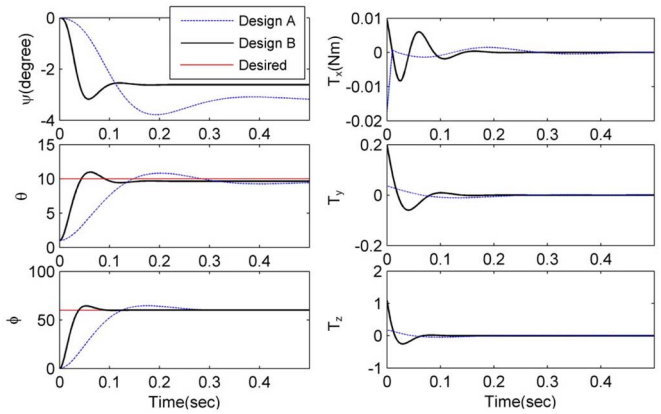

Fig. 13. Comparison of transient responses and torques.

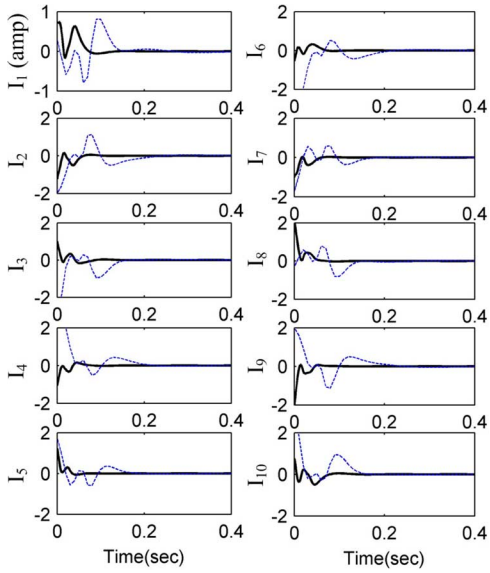

Fig. 14. Comparison of current inputs.

and transient responses of the two designs (Table III). The PD gains are set at $[K_p] = 550$[I], 3000[I], and $[K_d] = 30$[I], 140[I] for Designs A and B, respectively. Fig. 13 compares the transient responses to a step change in rotor orientation; the performance parameters and the required energy defined in (27) are summarized in Table VI.

$$H = \sum_{i=1}^{m_s} \int_{t_0}^{t} I_i(t) V_i(t)\, dt \tag{27}$$

where V_i and I_i are the voltage and the current, respectively, flowing through the ith pole pair. The comparison shows that Design B is superior to Design A in term of overshoot, response time, and current-to-torque ratio. Since Design B has a larger number of distributed coils and a better arrangement of coils and PMs, each coil demands a smaller input current, as compared in Fig. 14, which graphs the applied currents. This results in a much lower heat dissipation during transient provided that the final position can be maintained mechanically.

TABLE VI
TRANSIENT RESPONSE (ϕ) COMPARISON

	Design A	Design B
Overshoot (M_p, %)	6.7%	6.7%
Peak time (t_p, sec)	0.173	0.053
Rise time (t_r, sec)	0.134	0.037
Settling time (t_s, sec)	0.256	0.075
H (watts•sec)	7.55	4.34

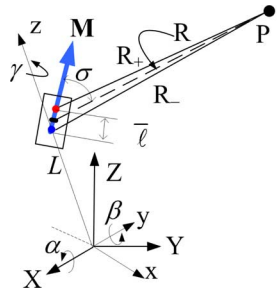

Location of sensor-pairs:

$$\mathbf{S}_{1\pm} = \begin{bmatrix} \pm S & 0 & Z_s \end{bmatrix}^{\mathrm{T}}$$

$$\mathbf{S}_{2\pm} = \begin{bmatrix} 0 & \pm S & Z_s \end{bmatrix}^{\mathrm{T}}$$

where S= 89mm (3.5in); and Z_s = 81mm (3.2in)

Fig. 15. Schematics illustrating inclination measurement.

VI. EXAMPLE 3: (INCLINATION SENSOR)

Fig. 15 illustrates the use of DMP models to determine the orientation (α, β) of an inclined shaft by measuring the $\mathbf{B}$-field of a moving cylindrical PM. Equation (9) provides a means to determine the unknown inclination $\mathbf{q}(\alpha, \beta)$ from the magnetic flux density $\mathbf{B}$, which can be measured using low-cost sensors such as the Hall effect sensor. The inverse problem can be solved from $B_{X\pm}$ and $B_{Y\pm}$ measured using two sensor pairs with location given in Fig. 15.

A common approach to reduce (9) for a real-time application is to compute the incremental change in orientation

$$\hat{\mathbf{q}} = \mathbf{q}_{k+1} - \mathbf{q}_k \tag{28}$$

such that $\mathbf{q}_{k+1}$at the $(k+1)$th time step is computed from its previous step $\mathbf{q}_k$ based on the perturbation model of (9)

$$[\mathbf{A}]\hat{\mathbf{q}} = \mathbf{b} \tag{29}$$

where

$$\hat{\mathbf{q}} = [\hat{\alpha} \quad \hat{\beta} \quad \hat{\gamma}]^{\mathrm{T}};\ \mathbf{b} = [\mathbf{B}(\mathbf{q}_{k+1}) - \mathbf{B}(\mathbf{q}_k)] \tag{30a,b}$$

and

$$[\mathbf{A}] = [\partial\mathbf{B}/\partial\alpha \quad \partial\mathbf{B}/\partial\beta \quad \partial\mathbf{B}/\partial\gamma]_{\mathbf{q}=\mathbf{q}_k} \in \mathbb{R}^{j\times 3}. \tag{30c}$$

For a sensor-located $\mathbf{P}$

$$\frac{\partial \mathbf{B}}{\partial q} = -\frac{\mu_o}{4\pi} \sum_{j=0}^{k} m_j \sum_{i=1}^{n_k} \frac{\partial}{\partial q} \left(\frac{\mathbf{R}_{\mathbf{ji}+}}{|\mathbf{R}_{\mathbf{ji}+}|^3} - \frac{\mathbf{R}_{\mathbf{ji}+}}{|\mathbf{R}_{\mathbf{ji}+}|^3} \right) \tag{31}$$

where q denotes α, β, or γ; and $\mathbf{R}_{\mathbf{ji}\pm} = \mathbf{P} - \mathbf{P}_{\mathbf{ji}\pm}$. The partial derivative in (31) is given by

$$\frac{\partial}{\partial q} \left(\frac{\mathbf{R}_{\mathbf{ji}\pm}}{|\mathbf{R}_{\mathbf{ji}\pm}|^3} \right) = -\frac{1}{|\mathbf{R}_{\mathbf{ji}\pm}|^3} \frac{\partial \mathbf{P}_{\mathbf{ji}\pm}}{\partial q} + \left(3\,[\mathbf{R}_{\mathbf{ji}\pm}]^T \frac{\partial \mathbf{P}_{\mathbf{ji}\pm}}{\partial q} \right) \frac{\mathbf{R}_{\mathbf{ji}\pm}}{|\mathbf{R}_{\mathbf{ji}\pm}|} \tag{31a}$$

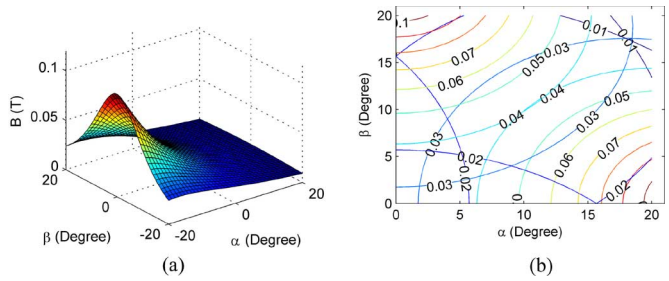

Fig. 16. Exact solutions and simulated measurements. (a) Analytical solution. (b) Simulated $B_{X\pm}$ and $B_{Y\pm}$.

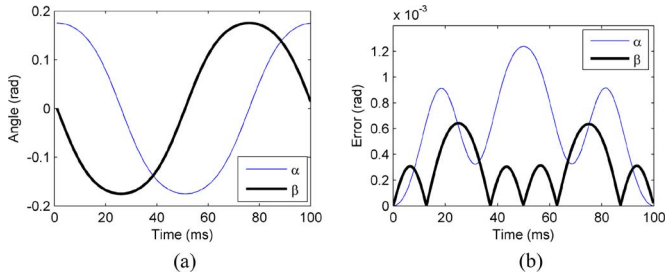

Fig. 17. Simulated circular motion and modeling errors. (a) α and β trajectory. (b) Modeling errors.

where

$$\partial \mathbf{P}_{ji\pm}/\partial q = \nabla\left[\Gamma(\mathbf{q})\mathbf{p}_{ji\pm}\right] \tag{32b}$$

and $\nabla = \partial/\partial\alpha + \partial/\partial\beta + \partial/\partial\gamma$. Hence, the orientation can be updated using (32)

$$\mathbf{q}_{k+1} = \mathbf{q}_k + \left([\mathbf{A}]^T[\mathbf{A}]\right)^{-1}[\mathbf{A}]^T\mathbf{b}. \tag{32}$$

Equation (32) provides the inverse solution of the field-based sensor system for incremental orientation measurement in real-time computation. Appendix B gives the Jacobian matrix $[\mathbf{A}]$ for a 2-DOF orientation (α, β) measurement.

Fig. 16(a) shows the simulated magnetic field $\boldsymbol{B_Y}$ at point $P(0, S, Z_s)$ using (9) over the (α, β) range of $\pm 20°$, for which the simulated measurements of constant $B_{X\pm}$ and $B_{Y\pm}$ contours (in Tesla) are plotted in Fig. 16(b). Fig. 17(a) and (b) shows the circular trajectory of the shaft inclined at 10° from the Z-axis, and the modeled measurement errors (in radians), respectively.

VII. Conclusion

We have introduced the distributed multipole (DMP) modeling method for design and control of PM-based devices. The DMP model extends the concept of a magnetic dipole model to account for the shape and magnetization of the physical magnet. Derived in closed form, we show how the DMP-models can be efficiently used to characterize the magnetic fields for computing magnetic forces and torques. The DMP method has been validated by comparing computed results against published experimental and numerical data. The simplicity of the DMP-based solutions along with precise (and yet intuitive) magnetic fields has been demonstrated with three practical examples of torque modeling and motion control simulation.

Appendix A
Equations of Rotor Motion

The motion of SWM can be characterized in term of ZYZ Euler angles $(\bar{\alpha}, \bar{\beta}, \gamma)$. For the mechanical structure, the equation of rotor motion derived using the Lagrangian formulation has the following form

$$[\mathbf{M}]\,\ddot{\mathbf{q}} + \mathbf{C}(\dot{\mathbf{q}}, \mathbf{q}) = \mathbf{Q} \tag{A1}$$

where

$$[\mathbf{M}] = \begin{bmatrix} (I_a - I_t)\cos^2\bar{\beta} + I_t & 0 & I_a\cos\bar{\beta} \\ 0 & I_t & 0 \\ I_a\cos\bar{\beta} & 0 & I_a \end{bmatrix} \tag{A2}$$

$$\mathbf{C}(\dot{\mathbf{q}}, \mathbf{q}) = \begin{bmatrix} 2(I_t - I_a)\sin\bar{\beta}\cos\bar{\beta}\dot{\bar{\alpha}}\dot{\bar{\beta}} - I_a\sin\bar{\beta}\dot{\bar{\beta}}\dot{\gamma} \\ (I_a - I_t)\sin\bar{\beta}\cos\bar{\beta}\dot{\bar{\alpha}}^2 + I_a\sin\bar{\beta}\dot{\bar{\alpha}}\dot{\bar{\beta}} \\ -I_a\sin\bar{\beta}\dot{\bar{\alpha}}\dot{\bar{\beta}} \end{bmatrix} \tag{A3}$$

and

$$\mathbf{Q} = \begin{bmatrix} -T_1\sin\bar{\beta}\cos\phi + T_2\sin\bar{\beta}\sin\gamma + T_3\cos\bar{\beta} \\ mgh\sin\bar{\beta} + T_1\sin\gamma + T_2\cos\gamma \\ T_3 \end{bmatrix} \tag{A4}$$

where $\mathbf{q} = [\bar{\alpha}\ \bar{\beta}\ \gamma]^T$; $I_a = I_{zz}$; $I_t = I_{xx} = I_{yy}$; and m is the mass of the rotor. In (A3), h accounts for the off-center of the mass; and $\mathbf{Q}$ represents the contributions of the applied torque to the generalized moments. The applied torque in the rotor frame is expressed by the stator frame as

$$\mathbf{T} = T_1\hat{i} + T_2\hat{j} + T_3\hat{k} \tag{A5}$$

where

$$\begin{aligned} T_1 &= T_X(\cos\bar{\alpha}\cos\bar{\beta}\cos\gamma - \sin\bar{\alpha}\sin\gamma) \\ &\quad + T_Y(\sin\bar{\alpha}\cos\bar{\beta}\sin\gamma + \cos\bar{\alpha}\sin\gamma) - T_Z\sin\bar{\beta}\cos\gamma \\ T_2 &= T_X(-\cos\bar{\alpha}\cos\bar{\beta}\sin\gamma - \sin\bar{\alpha}\cos\gamma) \\ &\quad + T_Y(-\sin\bar{\alpha}\cos\bar{\beta}\sin\gamma + \cos\bar{\alpha}\cos\gamma) + T_Z\sin\bar{\beta}\sin\gamma \\ T_3 &= T_X\cos\bar{\alpha}\sin\bar{\beta} + T_Y\sin\bar{\alpha}\sin\bar{\beta} + T_Z\cos\bar{\beta}. \end{aligned}$$

Appendix B
Jacobian Matrix of Magnetic Flux Density

The Jacobian matrix of the magnetic flux density $\mathbf{B}$ is given by (B1)

$$[\mathbf{A}] = \begin{bmatrix} \partial B_X/\partial\alpha & \partial B_X/\partial\beta \\ \partial B_Y/\partial\alpha & \partial B_Y/\partial\beta \end{bmatrix} = \frac{m}{\mathrm{D}^{5/2}}\begin{bmatrix} N_{X\alpha} & N_{X\beta} \\ N_{Y\alpha} & N_{Y\beta} \end{bmatrix} \tag{B1}$$

where

$$D = 2(X_1^2 + Y_1^2 + Z_1^2)$$

$$X_1 = X - xC_\beta - b_- S_\beta$$
$$Y_1 = Y - a_1$$
$$Z_1 = Z - xS_\beta + b_- C_\beta$$
$$a_1 = yC_\alpha + zS_\alpha, b_\pm = yS_\alpha \pm zC_\alpha$$

and the subscripts α and β of C and S denote cosine and sine of α and β, respectively and where

$$N_{X\alpha} = a_1 DS_\beta + 6X_1 \{-(a_1 S_\beta + zC_\alpha) X + b_- Y + a_1 C_\beta Z\}$$
$$N_{X\beta} = D[b_- C_\beta - xS_\beta] + 6X_1 [(xS_\beta - b_- C_\beta) X - (b_- S_\beta + xC_\beta) Z]$$
$$N_{Y\alpha} = -Db_+ + 6Y_1 [-(a_1 S_\beta + zC_\alpha) X + b_- Y + a_1 C_\beta Z]$$

and

$$N_{Y\beta} = 2^{-3/5} \mathrm{D}^2 (-b_- C_\beta + xS_\beta) + 6\, Y_1 [(C_\beta b_- - xS_\beta) X + (S_\beta b_- + xC_\beta) Z].$$

REFERENCES

[1] W. Clarke. (2002). *Mercedes-Benz F-400 Carving* [Online]. Available: edmunds.com.

[2] J. Peter, *The Wave of the Future?*. Dulles, VA: Wavecrest Laboratories LLC, Jan. 2004.

[3] K.-M. Lee and C. Kwan, "Design concept development of a spherical stepper for robotic applications," *IEEE Trans. Robot. Autom.*, vol. 7, no. 1, pp. 175–181, Feb. 1991.

[4] J. Wang, G. Jewell, and D. Howe, "Design and control of a novel spherical permanent magnet actuator with three degrees of freedom," *IEEE/ASME Trans. Mechatronics*, vol. 8, no. 4, pp. 457–468, Dec. 2003.

[5] Y. Liang, I. M. Chen, G. Yang, L. Wei, and K.-M. Lee, "Analytical and experimental investigation on the magnetic field and torque of a permanent magnet spherical actuator," *IEEE/ASME Trans. Mechatronics*, vol. 11, no. 4, pp. 409–419, Aug. 2006.

[6] R. F. Hanington, "Matrix methods for fields," *Proc. IEEE*, vol. 55, no. 2, pp. 136–149, Feb. 1967.

[7] T. J. Cui and C. H. Liang, "Perturbation technique for matrix equations and its application in the computation of internal fields in a three-dimensional arbitrarily shaped biological body," *IEEE Trans. Antennas Propag.*, vol. 42, no. 4, pp. 569–573, Apr. 1994.

[8] J. M. Johnson and R.-S. Yahya, "Genetic algorithms and method of moments (GA/MOM) for the design of integrated antennas," *IEEE Trans. Antennas Propag.*, vol. 47, no. 10, pp. 1606–1613, Oct. 1999.

[9] K.-M. Lee, R. A. Sosseh, and Z. Wei, "Effects of the torque model on the control of a VR spherical motor," *IFAC J. Control Eng. Pract.*, vol. 12, no. 11, pp. 1437–1449, Nov. 2004.

[10] Q. Li and K.-M. Lee, "An adaptive meshless computation method for design of electromechanical actuators," *IEEE Trans. Magn.*, vol. 42, no. 8, pp. 1996–2002, Aug. 2006.

[11] D. J. Craik, "Magnetostatics of axially symmetric structure," *J. Phys.*, vol. 7, pp. 1566–1573, 1974.

[12] M. A. Green, "Modeling the behavior of oriented permanent magnet material using current doublet theory," *IEEE Trans. Magn.*, vol. 24, no. 2, pp. 1528–1531, Mar. 1988.

[13] W. S. Bennett, "Basic sources of electric and magnetic fields newly examined," *IEEE Antennas Propag. Mag.*, vol. 43, no. 1, pp. 31–35, Feb. 2001.

[14] S. Nedelcu and J. H. P. Watson, "Magnetic dipole model of a permanent magnet based device," *J. Phys.*, vol. 34, no. 17, pp. 2622–2628, Sep. 2001.

[15] P. D. Visschere, "An exact two-dimensional model for a periodic circular array of head-to-head permanent magnets," *J. Phys. D, Appl. Phys.*, vol. 38, no. 3, pp. 355–362, Feb. 2005.

[16] I. Dufour and D. Placko, "An original approach to Eddy current problems through a complex electrical image concept," *IEEE Trans. Magn.*, vol. 32, no. 2, pp. 348–365, Mar. 1996.

[17] J. D. Jackson, *Classical Electrodynamics*. New York: Wiley, 1999.

[18] K.-M. Lee and H. Son, "Torque model for design and control of a spherical wheel motor," in *Proc. IEEE/ASME AIM 2005*, Jul., vol. 1, pp. 335–340.

[19] K.-M. Lee, Q. Li, and H. Son, "Effects of numerical formulation on magnetic field computation using meshless methods," *IEEE Trans. Magn.*, vol. 42, no. 9, pp. 2164–2171, Sep. 2006.

[20] K.-M. Lee, Q. Li, and W. Daley, "Effects of classification methods on color-based feature detection with food processing applications," *IEEE Trans. Autom. Sci. Eng.*, vol. 4, no. 1, pp. 40–51, Jan. 2007.

[21] K.-M. Lee and H. Son, "Distributed multipole model for design of permanent-magnet-based actuators," *IEEE Trans. Magn.*, vol. 43, no. 10, pp. 3904–3913, Oct. 2007.

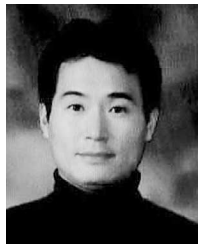

Hungsun Son (S'07) received the M.S. degree in aero and astronautical engineering from Stanford University, Stanford, CA, in 2002, and the Ph.D. degree in mechanical engineering from the Georgia Institute of Technology, Atlanta, in 2006.

He is currently a Senior Researcher with the IT Machinery Research Team in the Division of Intelligent Manufacturing and Systems at the Korea Institute of Machinery and Materials (KIMM). His current research interests include mechatronics, sensors and actuators, dynamic system modeling, design optimization, automation, and control.

Kok-Meng Lee (M'89–SM'02–F'05) received the M.S. and Ph.D. degrees in mechanical engineering from the Massachusetts Institute of Technology, Cambridge, MA, in 1982 and 1985, respectively.

Since 1985, he has been with the Faculty of Mechanical Engineering, Georgia Institute of Technology, Atlanta, where he is currenty a Professor of Mechanical Engineering. He is the holder of seven patents. His current research interests include system dynamics and control, machine vision, robotics, automation, and mechatronics.

Prof. Lee is a Fellow of the American Society of Mechanical Engineers. He has served on representative positions within the IEEE Robotics and Automation Society (RAS); he was Associate Editor of IEEE TRANSACTIONS ON ROBOTICS AND AUTOMATION during 1994–1998, *RAS Magazine* during 1994–1996, and IEEE TRANSACTIONS ON AUTOMATION SCIENCE AND ENGINEERING during 2003–2005, and Editor for the IEEE/ASME TRANSACTIONS ON MECHATRONICS during 1995–1999. In 2008, he is the Editor-in-Chief for the IEEE/ASME TRANSACTIONS ON MECHATRONICS. He served as Chair or Co-Chair for numerous international conferences. He was the recipient of numerous awards including the NSF Presidential Young Investigator (PYI) Award, Sigma Xi Junior Faculty Award, International Hall of Fame New Technology Award, Woodruff Faculty Fellow, three Best Paper Awards. He is also recognized as an Advisor for seven Best Student Paper Awards and a Best Thesis Award.